J. Fluid Mech. (1984), *vol.* 144, *pp.* 133–151
Printed in Great Britain

Pattern selection in single-component systems coupling Bénard convection and solidification

By S. H. DAVIS,
Department of Engineering Sciences and Applied Mathematics, Northwestern University, Evanston, Illinois 60201, USA

U. MÜLLER AND C. DIETSCHE
Kernforschungszentrum Karlsruhe GMBH, Institüt fur Reaktorbauelemente, Karlsruhe, West Germany

(Received 29 November 1983 and in revised form 28 February 1984)

A horizontal layer is heated from below and cooled from above so that the enclosed single-component liquid is frozen in the upper part of the layer. When the imposed temperature difference is such that the Rayleigh number across the liquid is supercritical, there is Bénard convection coupled with the dynamics of the solidification interface. An experiment is presented which shows that the interfacial corrugations that result are two-dimensional when this solid is thin but hexagonal when the solid is thick. A weakly nonlinear convective instability theory is presented which explains this behaviour, and isolates this 'purely thermal' mechanism of pattern selection. Jump behaviour is seen in the liquid-layer thickness at the onset of hexagonal convection.

1. Introduction

Convection can be the dominant mode of heat and mass transport in many processes that involve the freezing or melting of material. Such is the case for the storage of thermal energy based on the melting of the storage material. The solidification in moulds of liquid metals or alloys and the growth of crystals from melt or aqueous solutions are cases where double-diffusive processes may be present, so that there is the need to understand the interaction in multicomponent systems. Although the effect of convective transport in all these processes has been the subject of many experimental and theoretical investigations (see e.g. Foster 1969; Farhadieh & Tankin 1975; Fischer 1981; Saitoh & Hirose 1980, 1982; Hurle & Jakeman 1981; Marshall 1981), fundamental uncertainties exist in the prediction of the progress and the shape of the freezing or melting front.

The growth of crystals from binary solutions is a process where the interaction of adverse temperature and concentration gradients may generate unwanted interfacial instabilities during unidirectional solidification (Mullins & Sekerka 1964; Coriell *et al.* 1980; Coriell & Sekerka 1982). These instabilities generally deform the initially planar solid–liquid interface and lead to a cellular pattern of microsegregation. The interaction of the temperature and concentration fields near a progressing solidification front gives rise to the so-called morphological instability (Mullins & Sekerka 1964) in which convective effects are usually negligible. Weakly nonlinear theories (Wollkind & Segel 1970; Wollkind & Raissi 1974; Sriranganathan, Wollkind & Oulton 1983) lead to the prediction of hexagonal patterns for the resulting interfacial corrugations.

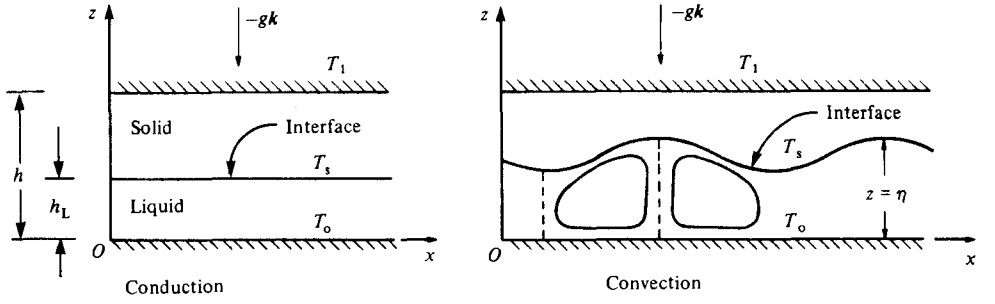

FIGURE 1. Schematic drawing of partially solidified liquid layer.

Interfacial instabilities may also originate from the onset of solutal or thermal convection in the liquid phase if the gradients are parallel to the gravity vector. Stability criteria based on linear analyses for solutal-driven convection have been given for various conditions by Hurle, Jakeman & Wheeler (1982, 1983). They also analyse the complex system of interacting morphological instabilities and solutal convection and show that stationary and oscillatory (overstable) perturbations of the temperature, concentration and velocity may occur when the critical conditions are exceeded.

In the present work we wish to focus on systems in which thermal convection and corrugations of a freezing/melting interface are strongly coupled. We consider a horizontal layer of a *single-component* liquid, cyclohexane, which is transparent, has no anomalous physical properties near its freezing point and whose thermal variations in physical properties are negligible. The layer is heated from below and the boundary temperatures adjusted so that the upper part is frozen and there is a solid–liquid interface. Depending on the Rayleigh number of the liquid, the heat in the liquid is transferred either by conduction only or by conduction and convection. The natural convection generally will occur in cellular form as it is observed in Bénard convection. If the heat is transported uniformly by conduction only, the interface between the solid and liquid layer will be planar; however, it will become corrugated if natural convection occurs in the liquid. The situation is sketched in figure 1.

Work on related systems is scarce. Yen (1968, 1980) performed experiments on melting ice blocks underneath or above a heated horizontal layer of water. He found regular patterns of corrugations at the ice surface. When the ice block was melted from below, he observed an array of small 'inverted hemispherical cells' at the ice surface. A pattern of axisymmetric troughs and crests occurred at the ice surface when the ice block was melted from above. No explanation was given for the occurrence of the different shapes of the interface deflections. The density anomaly of water at 4 °C may have had a major influence on the pattern formation.† Pantaloni *et al.* (1977) have obtained hexagonal planforms of solid–liquid interfaces in Rayleigh–Bénard experiments conducted with molten salts. They attribute the appearance of such patterns to the strong thermal variations of the viscosity in the fluid layer close to the solidification front. Such non-Boussinesq effects have been shown by Palm (1960), Segel & Stuart (1962), Segel (1965) and Busse (1967) to give rise to hexagonal convection in uncoupled systems. Pantaloni *et al.* (1977) implied that such convective

† Many papers are devoted to the details of the onset of convection in ice–water systems; these are summarized by Seki, Fukusako & Sugawara (1977).

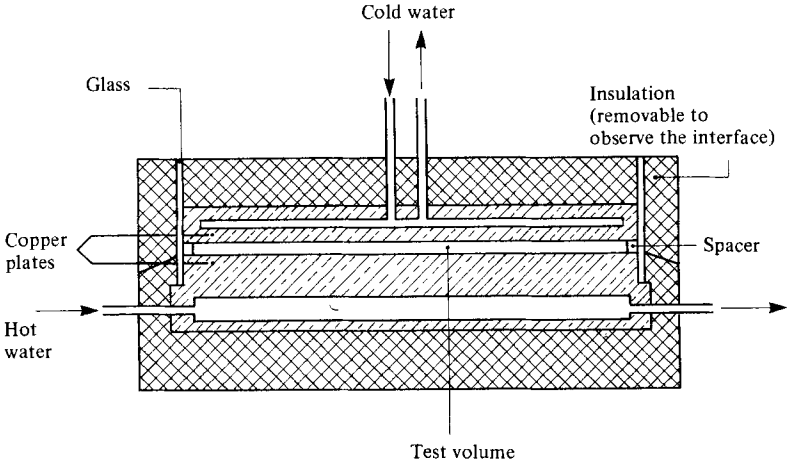

FIGURE 2. Experimental apparatus, layer height 4.18 mm or 5.04 mm.

patterns in the liquid generate the hexagonal corrugations at the solid–liquid interface.

It is the aim of the present investigation to identify the patterns of convective flow and interfacial corrugation, determine the parametric ranges in which different patterns occur and study the basic mechanics of the interfacial–flow interactions. In §2 we report on experiments that identify the corrugations of the interface. In §3 we perform a weakly nonlinear analysis of the coupled convective/interfacial system. We compare the theory and experiment and explain the mechanism of the pattern selection and the observations of the experiments. In §4 we summarize the study.

2. Experiments

2.1. *Apparatus and procedure*

The test apparatus is displayed schematically in figure 2. The test volume is bounded above and below by square copper plates of dimension 287 × 287 mm. The sidewalls consist of 5 mm thick glass plates. The distance between the horizontal plates is varied by placing small ceramic spacers of low heat conductivity at the rim of the plates. Spacers of height 4.18 mm and 5.04 mm are employed in the experiments. The manufacturing tolerances of both the flatness of the copper plates and the spacer heights are less than ± 0.02 mm. For temperature control the copper plates are put in direct contact with a system of meandering cooling channels at their lower and upper sides respectively. Coolant is provided from two high-precision thermostats of temperature deviation $\Delta T = \pm 0.01$ °C. The whole test chamber, including the connecting pipes to the thermostats, is insulated against external temperature perturbations by styrofoam plates and foam-rubber hoses.

For measuring the temperatures at the horizontal boundaries two Ni–Cr–Ni thermocouples are positioned in the upper copper plate and one in the lower plate, each 0.2 mm from the surface adjacent to the test volume. The same zero-point thermostat serves as a reference instrument for all thermocouples. Temperature fluctuations of less than ± 0.01 °C are assured. The thermoelectric voltage is amplified by differential amplifiers by a factor 1000 and displayed by a digital voltmeter.

Before starting the actual tests the thermocouples are calibrated by correlating the signals to the melting temperature of the test liquid, cyclohexane. The material

$\rho^{(L)} = 790.5$ kg/m^3,	$T_s = 6.38$ °C,
$\alpha = 1.17 \times 10^{-3}$ K^{-1},	$c_p^{(L)} = 1794$ J/(kg K),
$\lambda^{(L)} = 0.127$ W/mK,	$\mu = 1.26 \times 10^{-3}$ N s/m^2
$\lambda^{(S)}/\lambda^{(L)} = 1.07$,	

TABLE 1. List of material properties

properties of this liquid are listed in table 1. The calibration is performed by first reducing the temperature at the upper copper plate until a thin layer of solidified material of less than 0.1 mm is formed at the surface. Then the temperature is slowly raised until only a few tiny patches of the solid are seen on the surface. During this process the temperature of the lower copper plate is kept constant at 6.9 °C. An equivalent procedure is used for calibrating the thermocouple in the lower plate. This calibration is essential for obtaining the two main measured quantities, the temperature differences $T_0 - T_s$ and $T_s - T_1$.

Cyclohexane is chosen as the test liquid since the material properties are well known and no anomalies in material properties exist in the range 3–8 °C where the experiments have been carried out. Moreover, cyclohexane is transparent and exhibits a fixed melting temperature.

The structure of the solidification interface is directly viewed through observation slits at all four glass sidewalls. The reflection of this structure by the mirror-quality polished surface of the lower copper plate is an essential aid for the direct observation. However, for a photographic documentation the upper copper plate is removed from the test apparatus at certain fixed temperature levels of the lower and upper plates. Photos are then taken of the corrugated solidification interface under favourable lighting conditions. The removal of the plate must be rapid in order to avoid unwanted sublimation of the cyclohexane or condensation of water vapour from the air. Typically, photographs were taken between 30–60 s after the start of the dismantling of the apparatus.

2.2. *Observations*

We shall relate our observations to the case of pure heat conduction in which the solid–liquid interface is planar and its position is at $z = h_L$. This state is analysed in §3, where we find that

$$\frac{h - h_L}{h_L} = \frac{\lambda^{(S)}}{\lambda^{(L)}} \frac{T_s - T_1}{T_0 - T_s} \equiv A. \tag{2.1}$$

Here $\lambda^{(S)}$ and $\lambda^{(L)}$ are the thermal conductivities for the solid and liquid respectively, and for small A, A^{-1} turns out to be the equivalent Biot number for the heat transfer from the liquid to the solid. Notice that A also measures the amount of solid present.

We also introduce the Rayleigh number R to measure convection in the liquid. Here

$$R = \alpha g \frac{(T_0 - T_s) h_L^3}{\kappa^{(L)} \nu}, \tag{2.2}$$

where α is the volume expansion coefficient, g is the magnitude of the gravitational acceleration, $\kappa^{(L)}$ is the thermal diffusivity and ν is the kinematic viscosity.

In all experiments we keep T_0 fixed so that the temperature difference $T_0 - T_s$ is fixed, and we vary the temperature T_1 of the upper boundary. Thus, unlike the classical experiments in Bénard convection, the Rayleigh number is varied through changes in h_L, not through changes in the temperature difference.

Each experiment begins with a value of T_1 giving convection in the liquid. T_1 is then reduced slowly and in small steps. When T_1 reaches a value where the interface becomes planar, the state of pure conduction has replaced the state of convection. From here the experimental run is reversed by slowly increasing the temperature T_1 in small increments, keeping T_0 fixed, until the initial state of convection is reached again.† Different experimental runs lasted typically between 2 and 4 weeks. The rates of stepwise change of the temperature at the upper plate was 0.5 K/min, the state at each measuring point was stationary for at least 90 min before the data were taken.

Photographs of corrugated solid–liquid surfaces are shown in figure 3. Depending on the thickness of the solid layer, different patterns occur. If the solid layer is very thin, i.e. about 0.1 mm or less, roll-like patterns appear as shown in figure 3(*a*). A hexagonal pattern is generated for solid layers whose thicknesses are comparable with the depth of the liquid layer as shown in figure 3(*c*). In an intermediate range both polygonal and roll-like patterns are observed to coexist as displayed in figure 3(*b*).

The different states realized during two runs of experiments are shown in the graph of figure 4. Each state is characterized by two parameters R and A. For the upper curve the total layer depth $h = 5.04$ mm, whereas for the lower curve $h = 4.18$ mm. The range of different patterns of the solidified surface is characterized by the parameter A. We find two-dimensional patterns for $A < 0.05$ and hexagonal patterns for $A > 0.16$. For the intermediate range $0.05 < A < 0.16$ a mixed pattern of rolls and polygons is observed. The particular experimental trajectories obtained are due to the fact that variations in T_1 cause both R and A to vary simultaneously. Generally the different states could also be arranged under the condition of a constant Rayleigh number, though the temperatures at both copper plates would have to be varied simultaneously. As mentioned earlier, for reasons of experimental convenience, only the temperature of the upper plate was actually changed.

An analysis of the experimental errors has shown that the values of A for the transition between the different patterns are accurate within the following bounds:

$0.02 < A < 0.08$, roll-pattern/mixed-pattern transition;
$0.13 < A < 0.19$, mixed-pattern/hexagonal-pattern transition.

Our experimental observations lead to a physical mechanism for the generation of the patterns of corrugation that couple convective flow with interface deflection.

If the Rayleigh number of the liquid layer exceeds a critical value, cellular convection enhances the heat transfer in the liquid layer, which results in a partial melting of the solid. Since the convection cells are characterized by zones of up-flow and down-flow, the melting is not uniform. More solid is melted near the zones where warmer fluid rises toward the interface compared with zones where cold fluid sinks toward the lower boundary. This effect is displayed schematically in figure 1. It results in a formation of crests and troughs at the interface as observed in figure 3.

The surface deflection can lead to a degree of vertical asymmetry sufficient for hexagonal convection to be created, as shown by Davis & Segel (1968) for fluid–fluid interfaces. Our experimental observations indicate that this is the case when A is large. When A is small enough we see only roll-like patterns. We next outline a theory based on these ideas.

† In temperature ranges where qualitative changes in the flow behaviour were expected, the monotonic variations in the temperature T_1 were supplemented by cyclic variations in order to fix the temperature threshold of transitions.

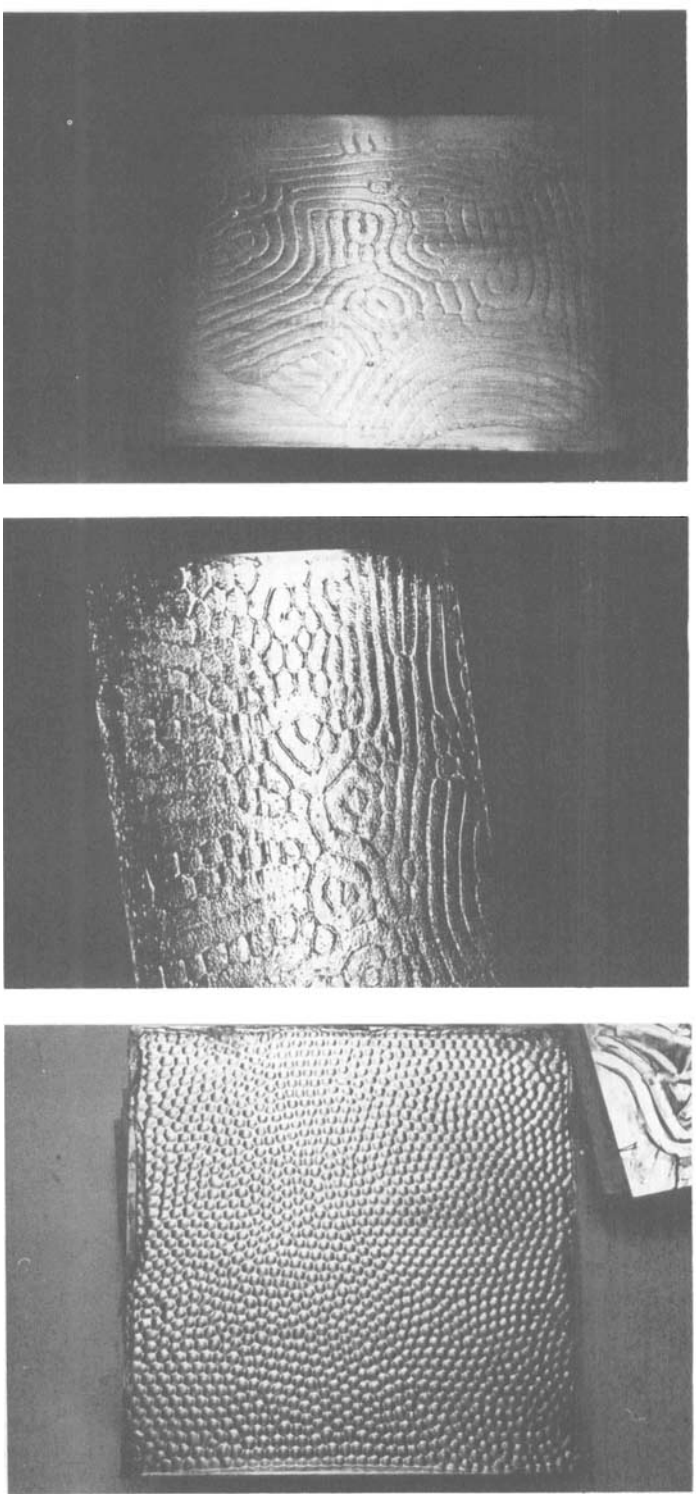

FIGURE 3. Photographs of corrugated solid–liquid interfaces: (*a*) roll-like pattern; (*b*) mixed polygonal–roll pattern; (*c*) hexagonal pattern.

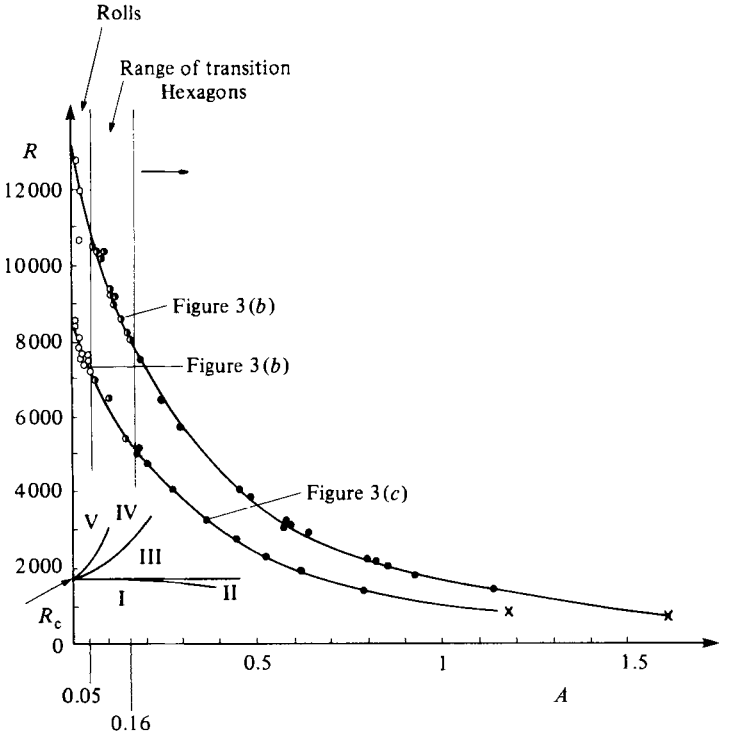

FIGURE 4. Regime diagram on the (R, A)-plane: labels I–V refer to critical values listed in (3.36); ○, rolls, ◑, rolls and polygons; ●, hexagons; ×, state of rest.

3. Theoretical model and analysis

3.1. *Formulation*

Consider the configuration sketched in figure 1 where the horizontal parallel plates at $z = 0$ and $z = h$ have infinite horizontal extent. The lower plate at $z = 0$ is fixed at the temperature $T = T_0$ while the upper plate at $z = h$ is fixed at temperature $T = T_1$. The material between the plates is a single-component liquid if $T > T_s$ and it is a solid if $T < T_s$. The layer is heated from below so that $T_1 < T_s < T_0$, and there is a solid–liquid interface at $z = \eta$ with $0 < \eta < h$. The material properties are the density ρ_0, the specific heat c_p, the thermal conductivity λ, diffusivity κ, kinematic viscosity ν, and the volume expansion coefficient α; superscripts S and L will be used to designate solid and liquid properties when required.

The coupled effects of buoyancy-driven convection and phase changes will be described by the heat equation in the solid and the Boussinesq equations (Mihaljan 1962) in the liquid. At the interface at $z = \eta$, we assume that there is no undercooling,† so that

$$T^{(L)} = T^{(S)} = T_s. \tag{3.1}$$

The jump in heat flux is balanced by the production of latent heat L,

$$\rho_0^{(S)} L \eta_t = [\lambda^{(S)} \nabla T^{(S)} - \lambda^{(L)} \nabla T^{(L)}] \cdot \boldsymbol{n} \tag{3.2}$$

† The Gibbs–Thompson effect includes the effect of interfacial energy γ by replacing (3.1) by $T^{(L)} = T^{(S)} = T_s + (\gamma/L) K$, where K is twice the mean curvature of the interface. We neglect this effect henceforth, though it is easily included.

where $\boldsymbol{n}$ is the unit normal vector to the interface:

$$\boldsymbol{n} = (-\eta_x, -\eta_y, 1)(1+\eta_x^2+\eta_y^2)^{-\frac{1}{2}}. \tag{3.3}$$

Subscripts x, y, z, t represent partial differentiation. The interface is non-mobile but deformable, so that there is the kinetic condition

$$\rho_0^{(\mathrm{L})}\boldsymbol{v}\cdot\boldsymbol{n} = [\rho_0^{(\mathrm{L})}-\rho_0^{(\mathrm{S})}](1+\eta_x^2+\eta_y^2)^{-\frac{1}{2}}\eta_t \tag{3.4}$$

and the no slip condition

$$\boldsymbol{v}\cdot\boldsymbol{t}^{(1)} = \boldsymbol{v}\cdot\boldsymbol{t}^{(2)} = 0, \tag{3.5}$$

where $\boldsymbol{t}^{(1)}$ and $\boldsymbol{t}^{(2)}$ are unit tangent vectors:

$$\boldsymbol{t}^{(1)} = (1+\eta_y^2, -\eta_x\eta_y, \eta_x)(1+\eta_x^2+\eta_y^2)^{-\frac{1}{2}}(1+\eta_y^2)^{-\frac{1}{2}}, \tag{3.6a}$$

$$\boldsymbol{t}^{(2)} = (0, 1, \eta_y)(1+\eta_y^2)^{-\frac{1}{2}}. \tag{3.6b}$$

The governing system possesses a *static equilibrium solution* in which the interface is planar at $z = \eta = h_{\mathrm{L}}$, the velocity vector $\boldsymbol{v}$ is identically zero, the pressure p is hydrostatic and the temperatures are purely conductive. Here

$$\bar{T}^{(\mathrm{L})} = T_{\mathrm{s}} - (T_0 - T_{\mathrm{s}})\frac{z-h_{\mathrm{L}}}{h_{\mathrm{L}}} \quad \text{and} \quad \bar{T}^{(\mathrm{S})} = T_{\mathrm{s}} - (T_{\mathrm{s}} - T_1)\frac{z-h_{\mathrm{L}}}{h-h_{\mathrm{L}}}. \tag{3.7a,b}$$

The fields (3.7) satisfy (3.1), $T^{(\mathrm{S})} = T_1$ at $z = h$ and $T^{(\mathrm{L})} = T_0$ at $z = 0$. The flux condition (3.2) further constrains the parameters so that

$$\frac{h_{\mathrm{S}}}{h_{\mathrm{L}}} = \frac{\lambda^{(\mathrm{S})}}{\lambda^{(\mathrm{L})}}\frac{T_{\mathrm{s}}-T_1}{T_0-T_{\mathrm{s}}} \equiv A, \tag{3.8}$$

where

$$h = h_{\mathrm{S}} + h_{\mathrm{L}}. \tag{3.9}$$

Thus the thicknesses of the solid and liquid layers are determined by T_0, T_1 and T_{s}. In particular, as $A \to 0$, the solid disappears.

We now introduce the following scales:

$$\left.\begin{aligned} x, y, z &\sim h_{\mathrm{L}}, \\ t &\sim h_{\mathrm{L}}^2/\kappa^{(\mathrm{L})}, \\ u, v, w &\sim \hat{W} \equiv [\kappa^{(\mathrm{L})}\alpha g h_{\mathrm{L}}(T_0 - T_{\mathrm{s}})/\nu]^{\frac{1}{2}}, \\ p &\sim \nu\rho_0^{(\mathrm{L})}\hat{W}/h_{\mathrm{L}}, \\ T - T_{\mathrm{s}} &\sim T_0 - T_{\mathrm{s}}. \end{aligned}\right\} \tag{3.10}$$

We use the same symbols as before to denote non-dimensional quantities; the full governing Boussinesq system is as follows:

$$T_t^{(\mathrm{L})} + R^{\frac{1}{2}}\boldsymbol{v}\cdot\nabla T^{(\mathrm{L})} = \nabla^2 T^{(\mathrm{L})}, \tag{3.11a}$$

$$P^{-1}[\boldsymbol{v}_t + R^{\frac{1}{2}}\boldsymbol{v}\cdot\nabla\boldsymbol{v}] = -\nabla p + \nabla^2\boldsymbol{v} + R^{\frac{1}{2}}T^{(\mathrm{L})}\boldsymbol{k}, \tag{3.11b}$$

$$\nabla\cdot\boldsymbol{v} = 0, \quad T_t^{(\mathrm{S})} = \kappa\nabla^2 T^{(\mathrm{S})}, \tag{3.11c,d}$$

$$\boldsymbol{v} = \boldsymbol{0}, \quad T^{(\mathrm{L})} = 1 \quad \text{on } z = 0, \tag{3.11e}$$

$$T^{(\mathrm{S})} = \lambda^{-1}A \quad \text{on } z = 1 + A, \tag{3.11f}$$

$$\left.\begin{aligned} \rho S\eta_t &= [\lambda\nabla T^{(\mathrm{S})} - \nabla T^{(\mathrm{L})}]\cdot\boldsymbol{n}, \quad T^{(\mathrm{L})} = T^{(\mathrm{S})} = 0, \\ (1-\rho)(1+\eta_x^2+\eta_y^2)^{-\frac{1}{2}}\eta_t &= \boldsymbol{v}\cdot\boldsymbol{n}, \quad \boldsymbol{v}\cdot\boldsymbol{t}^{(1)} = \boldsymbol{v}\cdot\boldsymbol{t}^{(2)} = 0, \end{aligned}\right\} \quad \text{on } z = \eta, \tag{3.11g,h / 3.11i,j}$$

where

$$\boldsymbol{k} = (0, 0, 1). \tag{3.11k}$$

Here (3.11 *a–c*) are the Boussinesq equations for the liquid and equation (3.11 *d*) gives the thermal field in the solid. The following non-dimensional groups emerge:

$$R = \frac{\alpha g(T_0 - T_s) h_L^3}{\kappa^{(L)} \nu}, \quad P = \frac{\nu}{\kappa^{(L)}}, \tag{3.12a, b}$$

$$\rho = \frac{\rho_0^{(S)}}{\rho_0^{(L)}}, \quad \lambda = \frac{\lambda^{(S)}}{\lambda^{(L)}}, \quad \kappa = \frac{\kappa^{(S)}}{\kappa^{(L)}}, \tag{3.12c, d, e}$$

$$S = \frac{\rho_0^{(L)} L \kappa^{(L)}}{\lambda^{(L)}(T_0 - T_s)}, \quad A = \frac{\lambda^{(S)}}{\lambda^{(L)}} \frac{T_s - T_1}{T_0 - T_s}. \tag{3.12f, g}$$

The main parameters that govern steady convection in the present system are R and A. Notice that owing to (3.8), a change in, say, T_1 causes both A and R to change simultaneously, the latter owing to the variation in h_L.

In non-dimensional terms, the basic state has $\boldsymbol{v} = \mathbf{0}$, p hydrostatic and

$$\bar{T}^{(L)} = 1 - z \quad (0 \leqslant z \leqslant 1) \quad \bar{T}^{(S)} = \lambda^{-1}(1 - z) \quad (1 \leqslant z \leqslant 1 + A). \tag{3.13a, b}$$

3.2. *Weakly nonlinear steady convection*

We wish to consider the basic state in which a slight rise in the temperature of the upper plate causes a slight melting of the solid. The increase in h_L, given that $T_0 - T_s$ is fixed, causes the Rayleigh number to pass through its critical value R_c leading to steady cellular convection of amplitude ϵ. We seek to describe this weakly nonlinear steady convection using a perturbation theory, first described by Malkus & Veronis (1958), by writing

$$\boldsymbol{v} = \mathbf{0} + \epsilon \boldsymbol{v}_1 + \epsilon^2 \boldsymbol{v}_2 + \ldots, \quad p = \bar{p} + \epsilon p_1 + \epsilon^2 p_2 + \ldots, \tag{3.14a, b}$$

$$T^{(L)} = \bar{T}^{(L)} + \epsilon T_1^{(L)} + \epsilon^2 T_2^{(L)} + \ldots, \quad T^{(S)} = \bar{T}^{(S)} + \epsilon T_1^{(S)} + \epsilon^2 T_2^{(S)} + \ldots, \tag{3.14c, d}$$

$$\eta = 1 + \epsilon \eta_1 + \epsilon^2 \eta_2 + \ldots, \tag{3.14e}$$

and representing

$$R = R_c + \epsilon R_1 + \epsilon^2 R_2 + \ldots \tag{3.15}$$

for all other parameters fixed. We substitute (3.14) and (3.15) into (3.11) and equate to zero coefficients of like powers of ϵ.

At order unity we reobtain the basic state. At order ϵ we obtain the linear stability problem under neutral conditions. We separate variables using normal modes:

$$(W_1, T_1^{(L)}, T_1^{(S)}, \eta_1) = (W_1(z), T_1^{(L)}(z), T_1^{(S)}(z), H_1)\, \Phi(x, y), \tag{3.16a}$$

where the planform function Φ satisfies

$$\Phi_{xx} + \Phi_{yy} = -k^2 \Phi \tag{3.16b}$$

and the usual normalization condition

$$\overline{\Phi^2} = 1. \tag{3.17}$$

Here the overbar denotes the horizontal average over one period in x and y, i.e. over one cell, and k is the overall wavenumber. The horizontal velocity components u_1 and v_1 can be written as

$$(u_1, v_1) = \frac{1}{k^2} \mathrm{D} W_1(z)\, (\Phi_x(x, y), \Phi_y(x, y)), \tag{3.18}$$

where $\mathrm{D} = \mathrm{d}/\mathrm{d}z$. Note that the planform function is arbitrary according to the linear theory, but is later determined by the stability properties of the weakly nonlinear steady-convection solutions.

The temperature field in the solid satisfies $\nabla^2 T_1^{(S)} = 0$ along with $T_1^{(S)}(x, y, 1+A) = 0$ and $T_1^{(S)}(x, y, 1) = \lambda^{-1}\eta$. We find that

$$T_1^{(S)}(z) = \lambda^{-1} H_1 \Lambda(\zeta) \tag{3.19}$$

where $$\zeta = \frac{z-1}{A} \quad \text{and} \quad \Lambda(\zeta) = \frac{\sinh kA(1-\zeta)}{\sinh kA}. \tag{3.20a,b}$$

The boundary conditions on temperature field in the liquid are the temperature and heat-flux conditions (3.11*g*, *h*) linearized about $z = 1$. These have the form

$$T_1^{(L)}(1) = H_1 \quad \text{and} \quad \mathrm{D}T_1^{(L)}(1) = -\mathscr{L} H_1. \tag{3.21a,b}$$

On the right-hand side of (3.21*b*) we have used (3.20), so that

$$\mathscr{L} = -A^{-1}\left[\frac{\mathrm{d}}{\mathrm{d}\zeta}\Lambda(\zeta)\right]_{\zeta=0} = k \coth kA. \tag{3.22}$$

The linear stability problem in the liquid governs Bénard convection under neutral conditions, which is conveniently written in an abstract notation. We follow Davis & Segel (1968) and write the four-vector

$$\boldsymbol{\Psi}_i = \begin{bmatrix} u_i \\ v_i \\ w_i \\ T_i^{(L)} \end{bmatrix}, \tag{3.23a}$$

and the linear operators

$$\boldsymbol{L} = \begin{bmatrix} \nabla^2 & 0 & 0 & 0 \\ 0 & \nabla^2 & 0 & 0 \\ 0 & 0 & \nabla^2 & 0 \\ 0 & 0 & 0 & \nabla^2 \end{bmatrix} \quad \text{and} \quad \boldsymbol{M} = \begin{bmatrix} 0 & 0 & 0 & 0 \\ 0 & 0 & 0 & 0 \\ 0 & 0 & 0 & 1 \\ 0 & 0 & 1 & 0 \end{bmatrix}. \tag{3.23b,c}$$

In terms of notation (3.23) the linear stability problem in the liquid written using the *primitive* equations can be posed as follows:

$$\{\boldsymbol{L} + R_c^{\frac{1}{2}}\boldsymbol{M}\}\cdot\boldsymbol{\Psi}_1 - \begin{bmatrix} p_{1x} \\ p_{1y} \\ p_{1z} \\ 0 \end{bmatrix} = \boldsymbol{0}, \quad \nabla\cdot\boldsymbol{v}_1 = 0. \tag{3.24a,b}$$

with the boundary conditions

$$u_1 = v_1 = w_1 = T_1^{(L)} = 0 \quad \text{on } z = 0 \tag{3.24c}$$

and $$u_1 = v_1 = w_1 = T_{1z}^{(L)} + \mathscr{L} T_1^{(L)} = 0 \quad \text{on } z = 1. \tag{3.24d}$$

The last condition in (3.24*d*) is obtained by eliminating H_1 (or equivalently η_1) between (3.21*a*) and (3.21*b*).

The conditions (3.24*d*) show that at the onset of convection the solid–liquid interface behaves like a planar rigid solid that is an *imperfect thermal conductor*. As A increases, this solid becomes a worse conductor, and as $A \to 0$, $\mathscr{L}^{-1} \sim A$, so that as the solid disappears the interface becomes a perfect thermal conductor.

The system (3.24) has a minimum critical Rayleigh number R_c which corresponds to $k = k_c$. In figures 5 and 6 we plot these as functions of A as obtained by a straightforward numerical integration. These are obtainable from the calculations of Nield (1968), even though we have a wavenumber-dependent 'Biot' number $\mathscr{L}$. In all theory that follows we take $k = k_c$ for each given B.

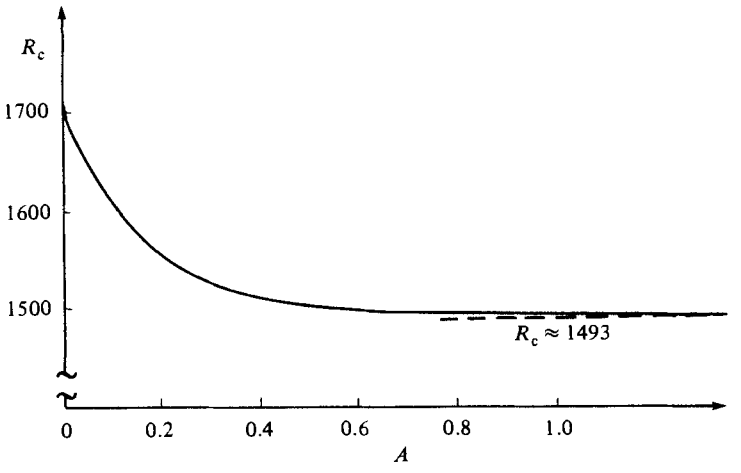

FIGURE 5. Critical Rayleigh number as a function of A.

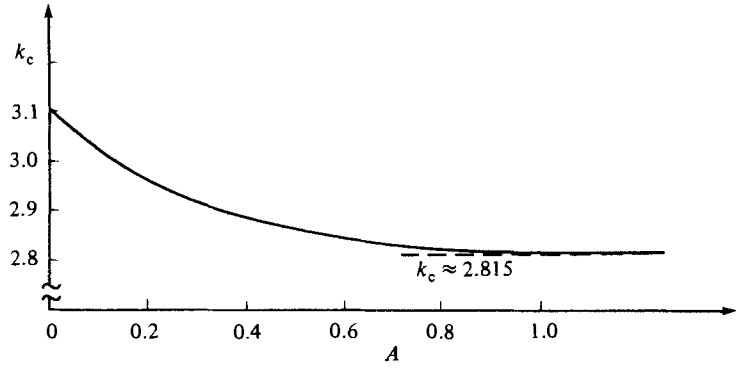

FIGURE 6. Critical wavenumber as a function of A.

It is easy to see that $\mathrm{D}T_1(1) < 0$, so from (3.21*b*) we have $H_1 > 0$. Thus there is a surface elevation ($H_1 > 0$) above a rising ($W_1 > 0$) convective current. This is consistent with the idea that the rising current is warm ($T_1 > 0$) so that more solid is melted here than at neighbouring points.

If we write the scalar product of two vectors $\boldsymbol{\Psi}_A$ and $\boldsymbol{\Psi}_B$ as

$$\langle \boldsymbol{\Psi}_A, \boldsymbol{\Psi}_B \rangle = \int_0^1 \overline{[u_A u_B + v_A v_B + w_A w_B + T_A^{(\mathrm{L})} T_B^{(\mathrm{L})}]}\, \mathrm{d}z, \tag{3.25}$$

then using the methods of Davis & Segel (1968), it is straightforward to show that the system (3.24) is self-adjoint.

We now turn to the $O(\epsilon^2)$ terms of the perturbation theory. In the solid, $\nabla^2 T_2^{(\mathrm{S})} = 0$ with $T_2^{(\mathrm{S})} = 0$ at $z = 1 + A$ and $T_2^{(\mathrm{S})} = \lambda^{-1}\eta_2 - T_{1z}^{(\mathrm{S})}\eta_1$ at $z = 1$. Thus

$$T_2^{(\mathrm{S})}(x, y, z) = \{\lambda^{-1}\eta_2 - T_{1z}^{(\mathrm{S})}|_{z=1}\,\eta_1\}\, \Lambda(\zeta), \tag{3.26}$$

and we find that the $O(\epsilon^2)$ Stefan condition becomes

$$T_{2z}^{(\mathrm{L})}(x, y, 1) = -\mathscr{L}(\eta_2 + \mathscr{L}\eta_1^2). \tag{3.27}$$

Hence we have used (3.19), (3.20), (3.22) and (3.26) as well as earlier relations on boundary conditions on the liquid at $z = 1$. Finally, we use $T_2^{(\mathrm{S})} - \lambda^{-1}\eta_2 + T_{1z}^{(\mathrm{S})}\eta_1 = 0$

on $z = 1$ to eliminate η_2 and find that $T_{2z}^{(L)} + \mathscr{L}T_2^{(L)} = 0$ at $z = 1$; here we have used (3.21*b*).

At order ϵ^2 the governing system in the liquid has the form

$$\{\boldsymbol{L} + R_c^{\frac{1}{2}}\boldsymbol{M}\}\cdot\boldsymbol{\Psi}_2 - \begin{bmatrix} p_{2x} \\ p_{2y} \\ p_{2z} \\ 0 \end{bmatrix} = R_c^{\frac{1}{2}} \begin{bmatrix} P^{-1}\boldsymbol{v}_1\cdot\nabla u_1 \\ P^{-1}\boldsymbol{v}_1\cdot\nabla v_1 \\ P^{-1}\boldsymbol{v}_1\cdot\nabla w_1 \\ \boldsymbol{v}_1\cdot\nabla T_1^{(L)} \end{bmatrix} - \tfrac{1}{2}R_c^{-\frac{1}{2}}R_1\boldsymbol{M}\cdot\boldsymbol{\Psi}_1 \tag{3.28a}$$

$$\nabla\cdot\boldsymbol{v}_2 = 0. \tag{3.28b}$$

The boundary conditions at $z = 0$ are

$$u_2 = v_2 = w_2 = T_2^{(L)} = 0 \quad \text{on } z = 0. \tag{3.28c}$$

The boundary conditions at $z = 1$ are obtained by referring the conditions on the deflecting interface to its mean position $z = 1$ and using the $O(\epsilon)$ conditions for simplifying the expressions. The final form requires a good deal of algebraic manipulation and leads to the following:

$$\left.\begin{aligned} u_2(x,y,1) &= -\eta_1(x,y)\,u_{1_z}(x,y,1), \\ v_2(x,y,1) &= -\eta_1(x,y)\,v_{1_z}(x,y,1), \\ w_2(x,y,1) &= 0 \\ T_{2z}^{(L)}(x,y,1) + \mathscr{L}T_2^{(L)}(x,y,1) &= 0. \end{aligned}\right\} \tag{3.28d}$$

We now apply the Fredholm alternative and take the scalar product of (3.28*a*) with $\boldsymbol{\Psi}_1$. From Davis & Segel (1968) we see that (i) the pressure-gradient terms vanishes, (ii) the nonlinear term vanishes, (iii) the terms involving the operator inversion, using Green's theorem, of $\boldsymbol{L} + R_c^{\frac{1}{2}}\boldsymbol{M}$ vanish except for the boundary integrals. In the latter terms we use conditions (3.28*c*, *d*) to reduce these. The result take the form

$$\tfrac{1}{2}R_c^{\frac{1}{2}}R_1\langle\boldsymbol{\Psi}_1, \boldsymbol{M}\cdot\boldsymbol{\Psi}_1\rangle = -\overline{\eta_1[u_{1_z}^2(x,y,1) + v_{1_z}^2(x,y,1)]}. \tag{3.29}$$

We now use the definitions of $\boldsymbol{\Psi}_1$ and $\boldsymbol{M}$ from (3.23) and the scalar product (3.25) to rewrite (3.29) as

$$R_1 = -R_c^{\frac{1}{2}}\frac{\overline{[\eta_1(u_{1_z}^2 + v_{1_z}^2)_{z=1}]}}{\int_0^1 \overline{w_1 T_1^{(L)}}\,\mathrm{d}z}. \tag{3.30}$$

Finally, we introduce the normal modes (3.16), use (3.18) and eliminate H_1 using (3.21*b*) to obtain

$$R_1 = \frac{R_c^{\frac{1}{2}}\mathscr{L}^{-1}[\mathrm{D}T_1^{(L)}(1)]\,[\mathrm{D}^2W_1(1)]^2}{k^4\int_0^1 W_1 T_1^{(L)}\,\mathrm{d}z}\,\frac{\overline{\Phi(\Phi_x^2 + \Phi_y^2)}}{\overline{\Phi^2}}. \tag{3.31}$$

The work of Schlüter, Lortz & Busse (1965), Segel (1965) and Busse (1967) has shown that stability considerations lead to the appearance of either roll cells or hexagons and that this nonlinear competition is contained in the following special form for Φ:

$$\Phi(x,y) = Y\cos\tfrac{1}{2}ky\cos\tfrac{1}{2}\sqrt{3}kx + Z\cos ky, \tag{3.32}$$

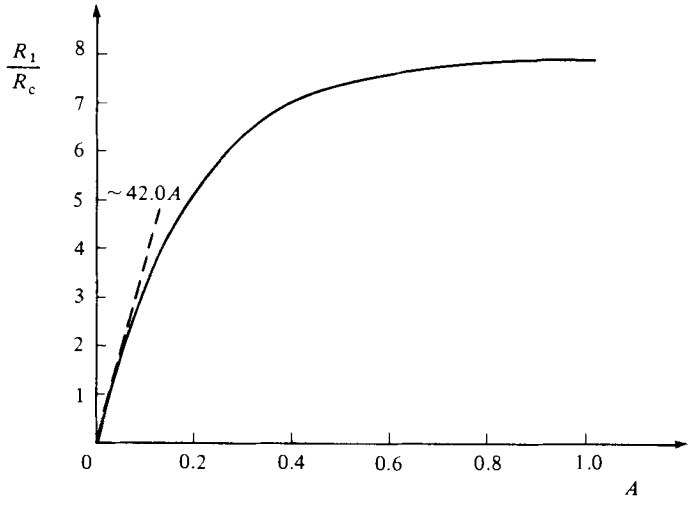

FIGURE 7. First-order correction R_1 of the Rayleigh number as a function of A.

where rolls have $Y = 0, Z \neq 0$ and hexagons have $Y = \pm 2Z$. The normalization (3.17) requires

$$\tfrac{1}{4}Y^2 + \tfrac{1}{2}Z^2 = 1, \tag{3.33}$$

so that $Z = \pm\sqrt{2}$ for rolls and $Z = \pm\sqrt{\frac{2}{3}}$ for hexagons.

The integration, giving the horizontal average, is zero for rolls, so that $R_1 = R_1^{(\mathrm{R})} = 0$ in this case, while for hexagons it gives $\pm\frac{1}{9}\sqrt{6}\,k^2$. Figure 7 shows $R_1 = R_1^{(\mathrm{H})}$ for hexagons with $Z > 0$ as a function of A. Here we have used the numerically computed eigenfunctions W_1 and $T_1^{(\mathrm{L})}$ to evaluate (3.31), and we have used the normalization $\max W_1(z) = 0.93848\,k_c^2(A)$.

At this stage we could obtain the $O(\epsilon^2)$ solutions, examine the $O(\epsilon^3)$ perturbation terms and formally obtain $R_2(A)$ for arbitrary A; this would then give us

$$R^{(\mathrm{H})} \sim R_c + R_1^{(\mathrm{H})}\epsilon + R_2^{(\mathrm{H})}\epsilon^2 \tag{3.34a}$$

for hexagons and

$$R^{(\mathrm{R})} \sim R_c + R_2^{(\mathrm{R})}\epsilon^2 \tag{3.34b}$$

for rolls. However, if A is not small, there is no justification for the retention in (3.34a) of the term $R_2^{(\mathrm{H})}\epsilon^2$, since it is obtained by perturbation theory in ϵ, which makes it formally negligible compared with $R_1^{(\mathrm{H})}\epsilon$. On the other hand, if A is small,† so that a double expansion in ϵ and A is permissible, then all three terms can be retained. Thus it is then justifiable to write

$$R_2^{(\mathrm{H})}(A) \sim R_2^{(\mathrm{H})}(0) = C^2 R_c[0.89360 + 0.04959\,P^{-1} + 0.06787\,P^{-2}], \tag{3.35a}$$

$$R_2^{(\mathrm{R})}(A) \sim R_2^{(\mathrm{R})}(0) = C^2 R_c[0.69942 - 0.00472\,P^{-1} + 0.00832\,P^{-2}], \tag{3.35b}$$

$$R_c(A) \sim R_c(0) = 1707.762, \quad k_c(A) \sim k_c(0) = 3.119 \tag{3.35c,d}$$

where

$$C^2 = R_c^{\frac{1}{2}} \int_0^1 W_1(z)\, T_1^{(\mathrm{L})}(z)\, \mathrm{d}z = 2904.4. \tag{3.35e}$$

† Equivalently, we could write $A = \bar{A}\epsilon$, where $\bar{A} = O(1)$ as $\epsilon \to 0$, and perturb in the single parameter ϵ. In this case for hexagons we would get $R \sim R_c + (R_{20} + R_{21}\bar{A})\epsilon^2$, where R_{20} would be equivalent to the $A = 0$ result of Schlüter *et al.* (1965) and R_{21} would be our $R_1^{(\mathrm{H})}(0)$; the results are thus identical.

The values given in (3.35a, b) were computed by Schlüter *et al.* (1965); we have inserted factors R_c and C^2 to account for the differences in non-dimensionalization and eigenfunction normalization between Schlüter *et al.* and us. We do so in (3.36) below as well. For small A, $\mathscr{L}^{-1} = O(A)$, so that (3.31) gives, consistent with figure 7,

$$R_1^{(H)}(A) \sim R_1^{(H)}(0) = -42.0\, R_c(0)\, A. \tag{3.35f}$$

From now on we use the symbol R_c to denote $R_c(0)$.

3.3. *Preferred mode*

The foregoing computation for steady convection leads to an infinite number of convective states, one for each Φ, which need to be distinguished by stability considerations. This has been done generally by Busse (1967) for cases where R_1 is small and generated by thermal variations in fluid properties. His stability analysis applies *directly* to our present work if A is small,† in which case four ranges of Rayleigh numbers exist for *stable* convective states. We can write these as follows:

$$\left.\begin{aligned}
&\text{I}\quad 0 < R < R_A = R_c - \frac{[R_1^{(H)}]^2}{4R_2^{(H)}} \quad \text{(pure conduction only)};\\
&\text{II}\quad R_A < R < R_c \quad \text{(pure conduction or hexagonal convection)};\\
&\text{III}\quad R_c < R < R_R = R_c + \frac{3R_2^{(R)}[R_1^{(H)}]^2}{C^4 R_c^2 L_2^2} \quad \text{(hexagonal convection only)};\\
&\text{IV}\quad R_R < R < R_B = R_c + \frac{[9R_2^{(H)} - 3C^2 R_c L_2][R_1^{(H)}]^2}{C^4 R_c^2 L_2^2}\\
&\qquad\qquad \text{(hexagonal convection or roll convection only)};\\
&\text{V}\quad R > R_B \quad \text{(roll convection only)};
\end{aligned}\right\} \tag{3.36}$$

where from Busse (1967) we have

$$L_2 = 0.29128 + 0.08147\, P^{-1} + 0.08932\, P^{-2}. \tag{3.37}$$

These ranges from the small-A theory have been drawn in figure 4 for $P \to \infty$. For purposes of clarity we have shown the curves for values of A larger than those appropriate for the perturbation theory. It is seen that the ranges divide the (R, A)-plane into sectors related to the observations though quantitative comparisons are not possible.

In range I pure conduction is the only stable steady state. In range II pure conduction is locally stable, but there can be a jump transition to stable hexagonal convection as indicated in the bifurcation plot of (3.34) on figure 8. Here a path $a \to b$ of increasing R results a jump to point c. If R increases further, hexagonal convection is maintained. However, if R is decreased along $c \to d$ then there is a jump down to pure conduction. Thus *abcd* constitutes a hysteresis loop. Since $R_1 < 0$ the hexagons that occur have upflow at their centres. Hexagons having downflow at their centres are unstable. In range III the same hexagons persist. In range IV both rolls and hexagons are stable, while in range V only rolls can persist. Again the path $a'b'c'd'$ constitute a hysteresis loop, this time involving jumps between hexagonal and roll convection.

† The interface deflection and the phase changes give rise to new local time derivatives (in the kinematic and Stefan boundary conditions) compared to the classical case. When A is small these terms do not alter the stability results of Busse (1967) nor the ranges listed above. However, if A is not small, then one does not know the result.

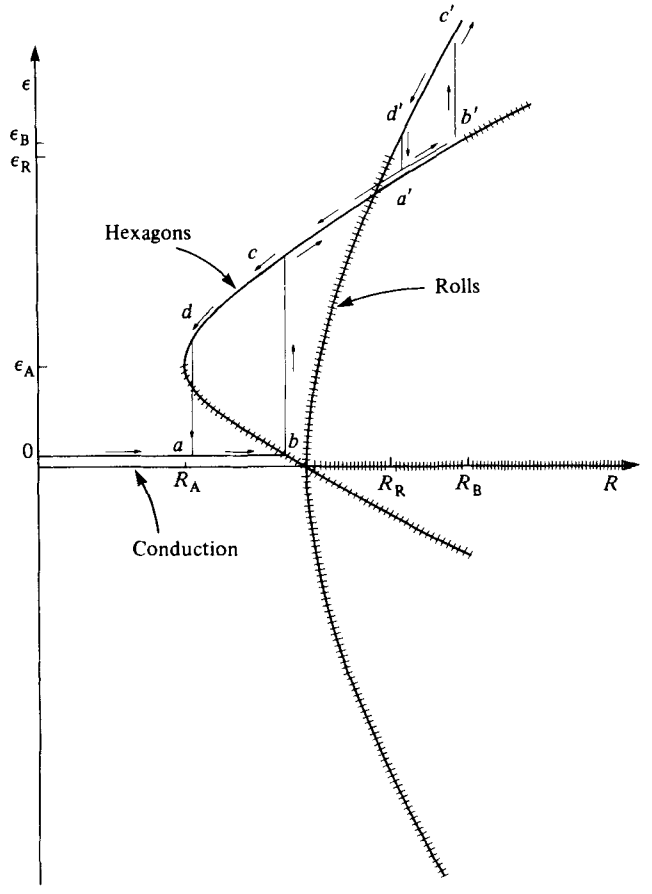

FIGURE 8. Sketch of the dependence of the amplitude on the Rayleigh number for rolls and hexagons, and bounds of stability; hatched curves mark unstable branches.

3.4. *Mean interface position*

The nonlinear theory for small A gives ranges for stable hexagons, rolls or both as listed in (3.36). The theory shows that the first hexagons seen (as R is increased) should occur through a jump as shown in figure 8. Thus a jump occurs somewhere between $R = R_A$ and $R = R_c$ and has magnitude between $R_1^{(H)}/2R_2^{(H)}$ and $R_1^{(H)}/R_2^{(H)}$. Given such a jump in ϵ, there should be an accompanying jump in convective heat transport (Nusselt number), which in turn would result in a jump in the mean position of the solidification interface.

We can examine this jump for small A by first solving for the $O(\epsilon^2)$ mean temperature $\bar{T}_2^{(L)}$. It satisfies

$$\mathrm{D}^2\bar{T}_2^{(L)} = R_c^{\frac{1}{2}}\mathrm{D}[W_1 T_1^{(L)}], \quad \bar{T}_2^{(L)}(0) = 0, \quad \mathrm{D}\bar{T}_2^{(L)}(1) + \mathscr{L}\bar{T}_2^{(L)}(1) = 0. \tag{3.38a, b, c}$$

We solve (3.38) to find that

$$\bar{T}_2^{(L)}(z) = R_c^{\frac{1}{2}}\left\{\int_0^z W_1 T_1^{(L)}\,\mathrm{d}z - \frac{z}{1+\mathscr{L}^{-1}}\left[\int_0^1 W_1 T_1^{(L)}\,\mathrm{d}z\right]\right\}. \tag{3.39}$$

We now average (3.27) over x and y to obtain

$$\mathrm{D}\bar{T}_2^{(L)}(1) = -\mathscr{L}(\bar{\eta}_2 + \mathscr{L}\overline{\eta_1^2}) = -\mathscr{L}(\bar{\eta}_2 + \mathscr{L}^{-1}[\mathrm{D}T_1^{(L)}(1)]^2), \tag{3.40}$$

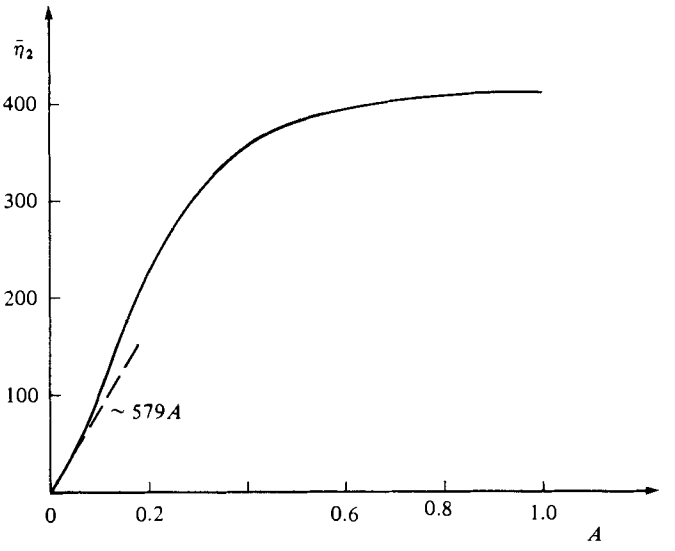

FIGURE 9. Second-order correction $\bar{\eta}_2$ for the average liquid-layer height as a function of A.

where we have used (3.16a), (3.17) and (3.21b). We now combine (3.39) and (3.40) to obtain

$$\bar{\eta}_2 = \mathscr{L}^{-1}\left\{\frac{R_c^{\frac{1}{2}}}{1+\mathscr{L}^{-1}}\int_0^1 WT_1^{(L)}\,dz - [DT_1^{(L)}(1)]^2\right\}. \tag{3.41}$$

The relation (3.41) is plotted in figure 9; for small A, $\bar{\eta}_2 \sim 579A$. Now, since $\eta \sim \epsilon\eta_1 + \epsilon^2\eta_2$, $\bar{\eta} \sim 1 + \epsilon^2\bar{\eta}_2$, and ϵ jumps in the range

$$\left(\frac{1}{2}\frac{R_1^{(H)}}{R_2^{(H)}}, \frac{R_1^{(H)}}{R_2^{(H)}}\right)$$

then for $A \to 0$ the mean jump $\bar{\eta} - 1 = O(A^3)$. Since $\bar{\eta}_2 > 0$, the onset of hexagonal convection is accompained by a *jump in mean thickness of the liquid layer.*

3.5. *Experimental/theoretical comparisons*

We have posed a theory for convection initiated by a slight melting of a solid and the subsequent convection coupled to the deflection of an interface sustaining changes of phase.

The linearized stability theory shows that in spite of the interface temperature being known *a priori*, the disturbances see an imperfectly conducting solid medium at $z = 1$. Linearized theory gives $R_c(A)$, which decreases by about 12.5% as A increases from zero to infinity. The critical wavenumber $k_c(A)$ decreases by about 9.7% over the same range. These values are consistent with the experimental observations. For example, our measurements of the hexagons in figure 3(c) gives $k = 3.0 \pm 0.2$ for $R = 3300$ and $A = 0.36$, while the linear theory for $R = R_c(0.36) \approx 1520$ and $k(0.36) \approx 2.9$. The rolls of figure 3(a) have $k = 2.5 \pm 0.1$ for $R = 7500$ and $A = 0.03$, qualitatively consistent with the wavenumber decreasing with increasing $R > R_c$.

The nonlinear theory for small A gives ranges for stable hexagons, rolls or both as listed in (3.36). The range of predicted hexagons approaches zero with A consistent

with the experimental observation that only roll cells are seen for small enough A ($A = 0.05$). For the value of $A = 0.05$ stable hexagons should be in the range

$$-4.2 \times 10^{-4} < \frac{R - R_c}{R_c} < 1.3 \times 10^{-1}, \tag{3.42}$$

which would be difficult to see by present techniques. However, when A is large, the range of stable hexagons should be large, consistent with the experimental observation that for A large enough ($A = 0.16$), well-formed hexagons or mixed polygonal states are always seen. For the value $A = 0.16$ stable hexagons should be in the range

$$-4.3 \times 10^{-3} < \frac{R - R_c}{R_c} < 1.3. \tag{3.43}$$

This range significantly exceeds the expected range of validity at our perturbation theory so that hexagons would be predicted 'always'!

The theory shows that the first hexagons seen should be present due to a jump from the conduction state. Figure 8 shows a bifurcation diagram of (3.34) for hexagons and rolls. As R is increased, the pure-conduction state loses stability through a jump of magnitude between $\frac{1}{2}R_1^{(H)}/R_2^{(H)}$ and $R_1^{(H)}/R_2^{(H)}$, which is $O(A)$ for small A. We have no experimental observations of such jumps in the *present* set-up, since viewing from the side of a thin, wide layer is difficult. However, in a subsequent experiment designed to focus on side-wall effects we have used identical materials but now a chamber having depth 10 mm and horizontal dimensions 20 mm × 200 mm. In these experiments $A = 5.0$ and we observe from the side a rapid jump in the mean position of the interface upon the onset of convection; the liquid layer *doubles* its thickness at the onset of convection. This is *not* an effect of changes of volume of the material upon solidification but one of the dynamical consequences of subcritical bifurcation.

We note that there is an alternative mechanism for the creation of hexagonal patterns as discussed by Palm (1960); Segel & Stuart (1962); Busse (1967) and Davis & Segel (1968). Here thermal variations, say $\Delta\mu$, across the liquid layer, of each fluid property μ, having mean value μ_0, lead to R_1 proportional to $\Delta\mu/\mu_0$. On one hand, cyclohexane closely satisfies the conditions of the Boussinesq approximation, so that $\Delta\mu/\mu_0$ is very small within the temperature change $T_0 - T_s \approx 1$ K. On the other hand, since $T_0 - T_s$ is fixed in the present experiment, independently of A, theories based on non-Boussinesq effects would predict a range of hexagons independent of A contrary to our observations. Thus such non-Boussinesq mechanisms are negligible in the present case.

4. Conclusions

In this paper we have examined a single-component liquid that solidifies at a known temperature T_s. The configuration involves a layer heated from below and cooled from above. A slight melting of the solid initiates steady thermal convection coupled to the deflection of an interface at which the changes in phase occur.

We have discussed an experiment in which large values of A (the ratio of solid to liquid thicknesses) lead to hexagonal convection that is readily observed, while small values of A lead to roll-like patterns. Presumably, stable hexagons do exist, but only in a Rayleigh-number range too small to be resolved experimentally.

We have discussed a theory for which small values of A are required since the perturbation theory is questionable when A is large.

We have compared experimental observation with theoretical prediction and found very good qualitative agreement in that (i) hexagonal convection and solid–liquid interface patterns predominate at large A, while two-dimensional convection and patterns are seen at small A; (ii) the wavenumber of the cells is consistent with a linear stability theory; (iii) the onset of hexagonal convection is accompanied by a jump in the mean position of the solid–liquid interface, so that the liquid depth suddenly increases.

The above agreement gives confidence that the coupled convective/phase-change system considered gives rise to hexagonal symmetries and that these states are driven by alterations in heat transfer at the interface due to interfacial deformation. Further, the prediction of upflow in the centres of the hexagonal cells fits the view that the phenomena are well-modelled by the theory. This 'purely thermal' mechanism should be present in other more complicated solidification systems in which buoyancy effects are appreciable.

The authors gratefully acknowledge the assistance of P. Damm during the performance of the experiments. S.H.D. was partially supported by a contract with the Army Research Office, Applied Mathematics Program.

REFERENCES

BUSSE, F. 1967 The stability of finite amplitude convection and its relation to an extreme principle. *J. Fluid Mech.* **30**, 625–649.

CORIELL, S. R., CORDES, M. R., BOETTINGER, W. J. & SEKERKA, R. F. 1980 Convective and interfacial instabilities during unidirectional solidification of a binary alloy. *J. Crystal Growth* **49**, 13–28.

CORIELL, S. R. & SEKERKA, R. F. 1982 Effect of convective flow on morphological stability. *Physico-Chem. Hydrodyn.* **2**, 281–293.

DAVIS, S. H. & SEGEL, L. A. 1968 Effects of surface curvature and property variation on cellular convection. *Phys. Fluids* **11**, 470–476.

FARHADIEH, R. & TANKIN, R. S. 1975 A study of the freezing of sea water. *J. Fluid Mech.* **71**, 293–304.

FISCHER, K. M. 1981 The effects of fluid flow on the solidification of industrial castings and ingots. *Physico-Chem. Hydrodyn.* **2**, 311–326.

FOSTER, T. D. 1969 Experiments on haline convection induced by the freezing of sea water. *J. Geophys. Res.* **74**, 6967–6974.

HURLE, D. T. J. & JAKEMAN, E. 1981 Introduction to the techniques of crystal growth. *Physico-Chem. Hydrodyn.* **2**, 237–244.

HURLE, D. T. J., JAKEMAN, E. & WHEELER, A. A. 1982 Effect of solutal convection on the morphological stability of a binary alloy. *J. Crystal Growth* **58**, 163–179.

HURLE, D. T. J., JAKEMAN, E. & WHEELER, A. A. 1983 Hydrodynamic stability of the melt during solidification of a binary alloy. *Phys. Fluids* **23**, 624–626.

MALKUS, W. V. R. & VERONIS, G. 1958 Finite amplitude cellular convection. *J. Fluid Mech.* **4**, 225–260.

MARSHALL, R. 1981 Experimental experience with the ASHRAE/NBS procedures for testing a phase change thermal storage device. In *Proc. Int. Conf. on Energy Storage, Brighton*, vol. 1, pp. 129–143.

MIHALJAN, J. M. 1962 A rigorous exposition of the Boussinesq approximation applicable to a thin layer of fluid. *Astrophys. J.* **136**, 1126–1133.

MULLINS, W. W. & SEKERKA, R. F. 1964 Stability of a planar interface during solidification of a dilute binary alloy. *J. Appl. Phys.* **35**, 444–451.

NIELD, D. A. 1968 The Rayleigh–Jeffreys problem with boundary slab of finite conductivity. *J. Fluid Mech.* **32**, 393–398.

PALM, E. 1960 On the tendency towards hexagonal cells in steady convection. *J. Fluid Mech.* **8**, 183–192.

PANTALONI, J., VELARDE, M. G., BAILLEUX, R. & GUYON, E. 1977 Sur la convection cellulaire dans les sels fondus pres de leur point de solidification. *C.R. Acad. Sci. Paris* **B285**, 275–278.

SAITOH, T. & HIROSE, K. 1980 Thermal instability of natural convection flow over a horizontal ice cylinder encompassing a maximum density point. *Trans. ASME* C: *J. Heat Transfer* **102**, 261–266.

SAITOH, T. & HIROSE, K. 1982 High Rayleigh number solutions to problems of latent heat thermal energy storage in a horizontal cylinder capsule. *Trans. ASME* C: *J. Heat Transfer* **104**, 545–553.

SCHLÜTER, A., LORTZ, D. & BUSSE, F. 1965 On the stability of steady finite amplitude convection. *J. Fluid Mech.* **23**, 129–144.

SEGEL, L. A. 1965 The nonlinear interaction of a finite number of disturbances to a layer of fluid heated from below. *J. Fluid Mech.* **21**, 359–384.

SEGEL, L. A. & STUART, J. T. 1962 On the question of the preferred mode in cellular thermal convection. *J. Fluid Mech.* **13**, 289–306.

SEKI, N., FUKUSAKO, S. & SUGAWARA, M. 1977 A criterion of onset of free convection in a horizontal melted water layer with a free surface. *Trans ASME* C: *J. Heat Transfer* **99**, 92–98.

SRIRANGANATHAN, R., WOLLKIND, D. J. & OULTON, D. B. 1983 A theoretical investigation of the development of interfacial cells during the solidification of a dilute binary alloy: comparison with the experiments of Morris and Winegard. *J. Crystal Growth* **62**, 265–283.

WOLLKIND, D. J. & RAISSI, S. 1974 A nonlinear stability analysis of the melting of a dilute binary alloy. *J. Crystal Growth* **26**, 277–293.

WOLLKIND, D. J. & SEGEL, L. A. 1970 A nonlinear stability analysis of the freezing of a dilute binary alloy. *Phil. Trans. R. Soc. Lond.* A **268**, 351–380.

YEN, Y.-C. 1968 Onset of convection in a layer of water formed by melting ice from below. *Phys. Fluids* **11**, 1263–1270.

YEN, Y.-C. 1980 Free convection heat transfer characteristics in a melt water layer. *Trans. ASME* C: *J. Heat Transfer* **102**, 550–556.